Underlying mechanism of charge transfer in Li-doped MgH_{16} at high pressure

Chongze Wang, Seho Yi, and Jun-Hyung Cho*
Department of Physics, Research Institute for Natural Science,
and HYU-HPSTAR-CIS High Pressure Research Center, Hanyang University,
222 Wangsimni-ro, Seongdong-Ku, Seoul 04763, Republic of Korea
(Dated: October 21, 2021)

A lithium-doped magnesium hydride Li_2MgH_{16} was recently reported [Y. Sun *et al*., Phys. Rev. Lett. **123**, 097001 (2019)] to exhibit the highest ever predicted superconducting transition temperature T_c under high pressure. Based on first-principles density-functional theory calculations, we reveal that the Li dopants locating in the pyroclore lattice sites give rise to the excess electrons distributed in interstitial regions. Such loosely bound anionic electrons are easily captured to stabilize a clathrate structure consisting of H cages. This addition of anionic electrons to H cages enhances the H-derived electronic density of states at the Fermi level, thereby leading to a high-T_c superconductivity. We thus propose that the electride nature of Li dopants is an essential ingredient in the charge transfer between Li dopants and H atoms. Our findings offer a deeper understanding of the underlying mechanism of charge transfer in Li_2MgH_{16} at high pressure.

PACS numbers:

I. INTRODUCTION

The realization of room-temperature superconductivity (SC) is one of the most challenging and very long standing issues in condensed matter physics [1]. For this issue, metallic hydrogen has been proposed [2] as an ideal system exhibiting the conventional Bardeen-Cooper-Schrieffer (BCS) type SC [3]. The lightest atomic mass in metallic hydrogen gives rise to high vibrational frequencies, which lead to achieving high T_c with strong electron-phonon coupling. However, it is very challenging to synthesize metallic hydrogen under extremely high pressures over ∼400 GPa [4–7] using diamond-anvil cells [8, 9]. In order to accomplish the metallization of hydrogen at relatively lower pressures, metal hydrides have been employed to utilize the so-called chemical precompression of hydrogen through metal elements [10]. Motivated by the theoretical predictions of high-T_c SC in a number of hydrides [11–18], experiments have been conducted to confirm that sulfur hydride H_3S exhibits a T_c of 203 K at pressures around 150 GPa [19] and more recently, lanthanum hydride LaH_{10} exhibits higher T_c around 250−260 K at ∼170 GPa [20, 21]. Therefore, the combined theoretical and experimental breakthroughs in high-pressure compressed hydrides have triggered a new era of high-T_c superconductors [1, 22–25].

To search for metal hydrides with higher T_c, there have been many theoretical studies of binary compounds including alkali metals [12–14], alkaline earth metals [15, 16], and rare earth metals [17, 18, 23, 24]. Recently, the realm of research has been extended to ternary compounds which may be more effective for achieving high-T_c SC because of an increase in the number of combinations of metal elements [26–28]. Based on first-principles density-functional theory (DFT) calculations and the Migdal-Eliashberg formalism, Yanming Ma and his colleagues predicted that a ternary hydride Li_2MgH_{16} exhibits a T_c of ∼473 K at 250 GPa [26]. Such highest ever predicted T_c was enabled by Li doping in a binary hydride MgH_{16} containing a large amount of H_2 molecules. Here, the supply of extra electrons via Li doping breaks the strong covalent bond of H_2 molecules to stabilize the clathrate H cages with weakly covalent H−H bonds. The resulting H network enhances the H-derived electronic density of states (DOS) at the Fermi level E_F, giving rise to a high-T_c SC. It is natural that the charge transfer from Li dopants to H atoms in Li_2MgH_{16} would be induced by a much lower electronegativity of Li atom compared to H atom [26].

The concept of electronegativity describes the tendency of an atom to attract electron density towards itself. The electronegativity χ is usually assumed to be similar values in a variety of chemical environments. It is, however, noted that a recent quantum-mechanical model study [29] reported a significant variation of χ under pressure. Meanwhile, at high pressure, some materials behave as electrides, where some excess electrons are transferred from positively charged ions to interstitial regions [30–32]. Such loosely bound anionic electrons are here demonstrated to play an important role in the charge transfer process between Li dopants and H atoms in Li_2MgH_{16}.

In the present study, we propose the underlying mechanism behind the charge transfer from Li dopants to H atoms in Li_2MgH_{16}. Using first-principles DFT calculations, we reveal that the Li dopants locating in the pyroclore lattice sites exhibit an electride feature with the anionic electrons residing in interstitial regions. Such loosely bound anionic electrons are easily captured to stabilize the clathrate H cages composed of two H species, H_1 and H_2 [see Fig. 1(a)]. It is thus likely that anionic electrons play an essential role in the charge transfer from Li dopants to H atoms. Our findings demonstrate that the anionic electrons created by the pyroclore-structured Li dopants are of vital importance not only for stabilizing the clathrate H cages, but also for enhancing the H-derived DOS at E_F. The presently proposed charge transfer mechanism via anionic electrons can be also applied for compressed LaH_{10} [20, 21], and hence, it is anticipated to be more generic to other compressed high-T_c superconducting hydrides with

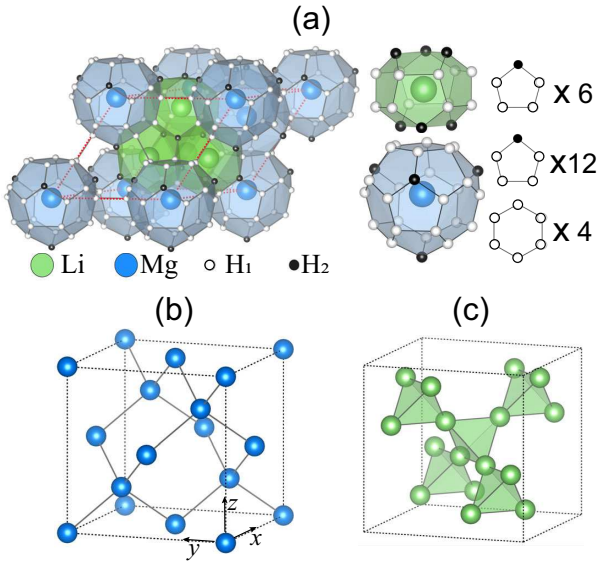

FIG. 1: (Color online) (a) Optimized clathrate structure of Li_2MgH_{16} consisting of Li-encapsulated H_{18} cages and Mg-encapsulated H_{28} cages. The H_{18} cage consists of six pentagon rings, while the H_{28} cage consists of twelve pentagon and four hexagon rings. There are two species of H atoms (designated as H_1 and H_2). The diamond lattice of Mg atoms and the pyroclore lattice of Li dopants are displayed in (b) and (c), respectively. The primitive unit cell with the lattice parameters a, b, and c is shown in (a), while the conventional unit cell is shown in (b) and (c). In (b), the x, y, and z axes point along the [001], [010], and [001] directions, respectively.

clathrate structures.

II. COMPUTATIONAL METHODS

Our DFT calculations were performed using the Vienna *ab initio* simulation package with the projector-augmented wave method [33–35]. Here, we included Li-$1s^2 2s^1$, Mg-$2s^2 2p^6 3s^2$, and H-$1s^1$ electrons in the electronic-structure calculations. For the exchange-correlation energy, we employed the generalized-gradient approximation functional of Perdew-Burke-Ernzerhof (PBE) [36]. A plane-wave basis was taken with a kinetic energy cutoff of 850 eV. The **k**-space integration was done with 16×16×16 k points (in the Brillouin zone) for the structure optimization and 32×32×32 k points for the DOS calculation. All atoms were allowed to relax along the calculated forces until all the residual force components were less than 0.001 eV/Å. Using the QUANTUM ESPRESSO package [37, 38], we calculated phonon frequencies with 4×4×4 q points.

III. RESULTS

We first optimize the geometry of Li_2MgH_{16} at a pressure of 300 GPa [26], which has a clathrate structure with the high

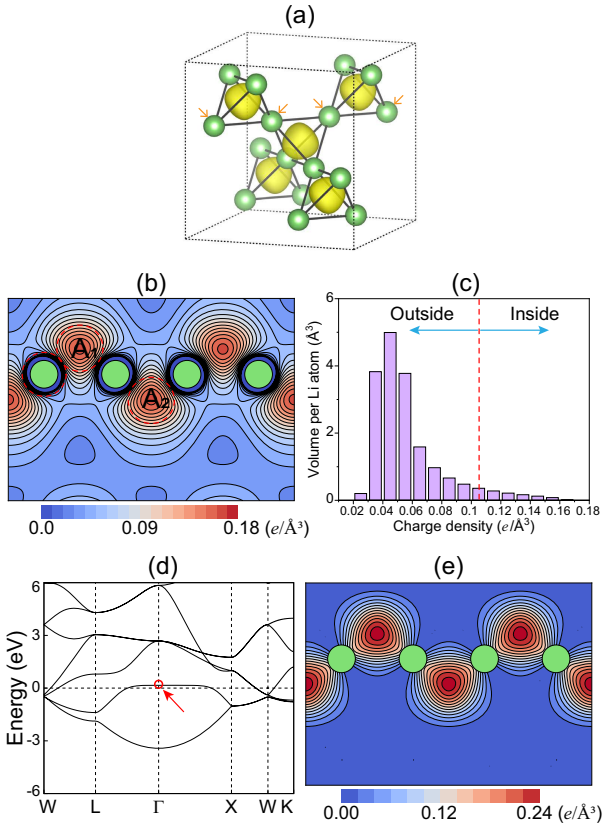

FIG. 2: (Color online) (a) Isosurface and (b) contour plots of valence charge density of the isolated Li dopants with the pyroclore structure. The isosurface level in (a) is 0.12 e/Å^3, and the contour spacing in (b) is 0.01 e/Å^3. In (b), the contour plot is drawn on the (110) plane containing Li atoms indicated by the arrows in (a). The dashed circles in (b) represent the MT spheres around the Li atom with a radius of 0.713 Å as well as around the A_1 and A_2 sites with a radius of 0.75 Å. The histogram of volume distribution for every charge density range of 0.01 e/Å^3 is given in (c), where "Outside" and "Inside" represent the charge density ranges outside and within the MT spheres around the A_1 and A_2 sites, respectively. The band structure of isolated Li dopants is displayed in (d). In (e), the charge density of the lowest unoccupied state at the Γ point [indicated by the arrow in (d)] is plotted on the (110) plane with a contour spacing of 0.02 e/Å^3.

crystalline symmetry of space group $Fd\bar{3}m$ [see Fig. 1(a)]. The optimized lattice parameters of the primitive unit cell are $a = b = c = 6.572$ Å. It is noted that Mg atoms form a diamond lattice [see Fig. 1(b)], while Li dopants form a pyroclore or three-dimensional (3D) kagome lattice [see Fig. 1(c)]. As shown in Fig. 1(a), there are two kinds of H cages: i.e., one is the H_{18} cage surrounding a Li atom and the other is the H_{28} cage surrounding a Mg atom. The H_{18} cage consisting of six pentagon rings is opened to connect to neighboring H_{18} cages, but the H_{28} cage consisting of twelve pentagon and four hexagon rings has a closed shape [see Fig. 1(a) and Fig. S1 in the Supplemental Information [39]]. The two cages are formed by two species of H atoms, H_1 (equivalent to H_{96g} in Ref. [26]) and H_2 (equivalent to H_{32e}). We find

that the H_1-H_1 bond length d_1 ($d_{1'}$) is 1.195 (1.023) Å, while the H_1-H_2 bond length d_2 is 1.084 Å. Note that the longer H_1-H_1 bond arises from the pentagon ring, while the shorter one is shared by the pentagon and hexagon rings (see Fig. S1 in the Supplemental Information [39]). These values of d_1, $d_{1'}$, and d_2 are in good agreement with those (d_1 = 1.20, $d_{1'}$ = 1.02 Å, and d_2 = 1.08 Å) of a previous DFT calculation [26].

Figure 2(a) shows the valence charge-density isosurface of the isolated Li dopants [see Fig. 1(c)] whose structure is taken from the optimized structure of Li_2MgH_{16}. Since the Li-1s core state is located at around −46.6 eV below E_F [see Fig. S2(a) in the Supplemental Information [39]], we exclude the $1s^2$ core electrons to plot the valence charge density. It is noted that each Li atom in Fig. 2(b) has ∼0.08 electrons within the muffin-tin (MT) sphere having a radius of 0.713 Å [close to the size of the corresponding Bader basin in Li_2MgH_{16}: see Fig. 3(d)], indicating that Li loses about 0.92 electrons. Interestingly, we find that some electrons detached from Li atoms are well distributed in the interstitial regions surrounded by four adjacent Li atoms [see Fig. 2(a)]. The confinement of such anionic electrons around the A_1 and A_2 sites is confirmed by the electron localization function [40] (see Fig. S3 in the Supplemental Material [39]), which is effective for the characterization of interstitial electrons in electride materials [41–43]. It is, however, noticeable that anionic electrons arising from Li dopants are extensively distributed over the regions within and outside the MT spheres around the A_1 and A_2 sites [see Fig. 2(b)]. Figure 2(c) shows the histogram of volume distribution for every charge density range of $0.01e/Å^3$. This histogram reveals that, although anionic electrons have the highest densities at the A_1 and A_2 sites, they occupy more volume outside the MT spheres around the A1 and A2 sites compared to within the MT spheres. In order to examine how anionic electrons arising from Li dopants change as a function of pressure, we compare the valence charge densities of the isolated Li dopants at 250, 300, and 350 GPa, respectively (see Fig. S4 in the Supplemental Information [39]). We find that the charge density at the A_1 or A_2 site increases as 0.158, 0.164, and 0.170 $e/Å^3$ at 250, 300, and 350 GPa, respectively, reflecting that anionic electrons around the A_1 and A_2 sites increase more dominantly with increasing pressure. It is thus likely that more anionic electrons can be captured to H cages with increasing pressure. Consequently, the H_1-H_1 and H_1-H_2 bond lengths are calculated to be shortened as (d_1, $d_{1'}$, d_2) = (1.229, 1.043, 1.106), (1.195, 1.023, 1.084), and (1.168, 1.006, 1.065) Å at 250, 300, and 350 GPa, respectively. Based on these results, we can say that the Li dopants locating in the pyroclore lattice sites possess the electride characteristics with the A_1 and A_2 anions.

In Fig. 2(d), we present the band structure of the pyroclore-structured Li dopants. It is seen that one band is fully filled but three bands are partially filled, with four valence electrons coming from four Li atoms in the primitive unit cell. Specifically, one band exhibits a partially flat dispersion at ∼0.1 eV above E_F. The charge character of this flat band at the Γ point represents strongly localized electrons at the interstitial regions surrounded by adjacent four Li atoms [see Fig. 2(e)], much larger than the total valence charge density shown in Fig. 2(b). Such a flatband nature of localized electrons is likely attributed to the geometric character of 3D kagome lattice, which hosts the destructive interferences of Bloch wave functions [44]. The destructive interfered electrons producing dispersionless flatbands have been theoretically proposed in 2D kagome lattices [45], and their existence has been experimentally observed in real materials [44]. We note that, despite the localized character of such interstitial electrons, the pyroclore-structured Li dopants show metallic behavior with multiple dispersive bands crossing E_F [see Fig. 2(c)].

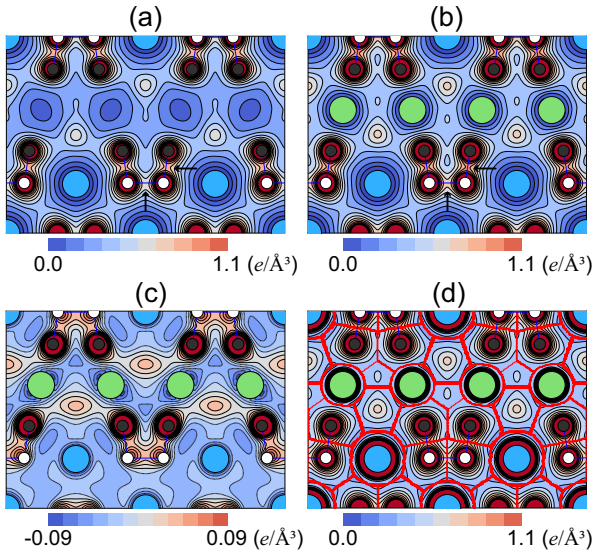

FIG. 3: (Color online) Calculated valence charge densities of (a) the parent MgH_{16} system and (b) Li_2MgH_{16}. The charge densities are drawn on the (110) plane with a contour spacing of 0.11 $e/Å^3$. The charge density difference Δρ (defined in the text) is displayed in (c) with a contour spacing of 0.015 $e/Å^3$. In (d), the Bader basins of Li_2MgH_{16}, obtained from the gradient of total charge density, is displayed.

Next, we explore the charge density of the parent MgH_{16} system whose structure is taken from the optimized structure of Li_2MgH_{16}. Since the Mg-2s(2p) semicore states located at −77.8(−44.6) eV below E_F are well separated from the valence states [see Fig. S2(b) in the Supplemental Information [39]], we exclude such semicore electrons to plot the valence charge density of MgH_{16} in Fig. 3(a). It is seen that H atoms in the H_{18} and H_{28} cages are bonded to each other with covalent bonds. We note that each H−H bond has a saddle point of charge density at its midpoint, similar to the C−C covalent bond in diamond [46]. The charge densities at the midpoints of the H_1-H_1 and H_1-H_2 bonds are 0.60 and 0.80 $e/Å^3$, respectively [see the arrows in Fig. 3(a)]. It is, however, noticeable that the calculated phonon spectrum of MgH_{16} exhibits imaginary frequencies in the whole Brillouin zone [see Fig. S5(a) in the Supplemental Material [39]], indicating that the MgH_{16} structure without Li atoms is dynam-

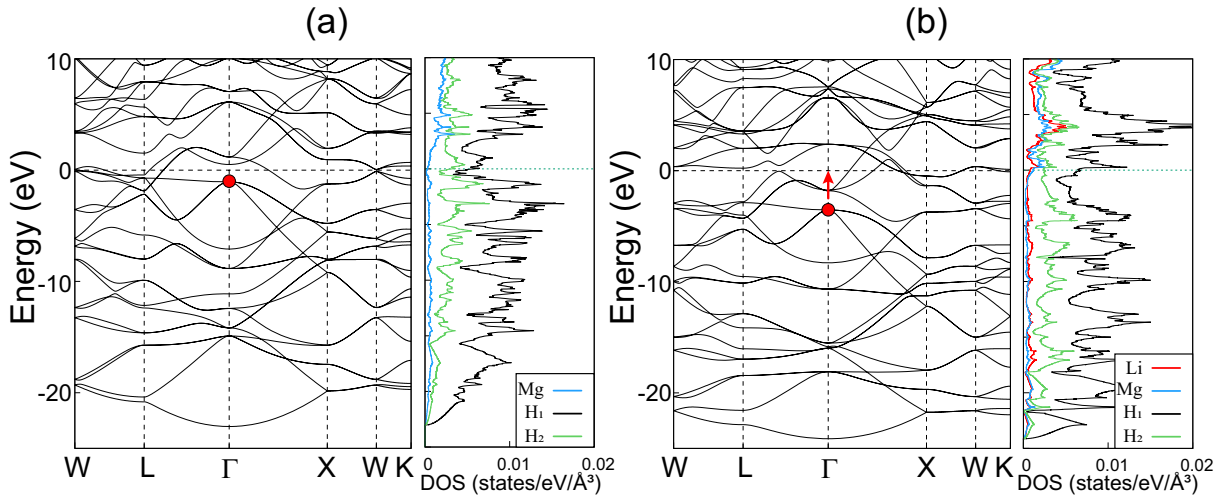

FIG. 4: (Color online) Calculated band structures of (a) the parent MgH_{16} system and (b) Li_2MgH_{16}, together with the corresponding LDOS of Mg/Li and H atoms. For the LDOS calculation, we choose the radii of muffin-tin spheres around Mg, Li, and H atoms as 0.94, 0.72 and 0.53 Å, respectively. The energy zero represents E_F. In (a), the highest occupied state at the Γ point is marked with the red circle. In (b), the arrow indicates the shift of E_F, relative to the parent MgH_{16} system.

ically unstable. We further relax the structure of MgH_{16} to find a saddle point. The calculated phonon spectrum of such a saddle point structre also shows imaginary-frequency phonon modes [see Fig. S5(b)], indicating that it is still dynamically unstable. Meanwhile, the Li_2MgH_{16} structure is dynamically stable without any imaginary-frequency mode [see Fig. S5(c) in the Supplemental Information [39]]. It is thus likely that the stability of H cages in Li_2MgH_{16} is enabled by capturing the anionic electrons in the pyroclore-structured Li dopants, as discussed below.

Figure 3(b) shows the calculated valence charge density $\rho_{Li/MgH}$ of Li_2MgH_{16}, where the charge densities at the mid-points of the H_1-H_1 and H_1-H_2 bonds are 0.69 and 0.90 e/Å^3, respectively [see the arrows in Fig. 3(b)]. These values are larger than the corresponding ones (0.60 and 0.80 e/Å^3) in MgH_{16}, because the anionic electrons of the pyroclore-structured Li dopants are captured to the H_{18} and H_{28} cages. It is interestingly noticeable that the charge transfer from Li dopants to H atoms was interpreted in terms of a lower electronegativity of Li atom compared to H atom [26]. By contrast, we here propose that the electride nature of Li dopants is an essential ingredient in the charge transfer between Li dopants and H atoms, thereby providing new insight into understanding the charge transfer mechanism in Li_2MgH_{16}. In order to examine the charge transfer from the Li dopants to H cages, we calculate the charge density difference, defined as $\Delta\rho = \rho_{Li/MgH} - \rho_{Li} - \rho_{MgH}$, where ρ_{Li} and ρ_{MgH} represent the separated charge densities of Li dopants [see Fig. 2(b)] and parent MgH_{16} [see Fig. 3(a)], respectively. As shown in Fig. 3(c), $\Delta\rho$ illustrates that electronic charge is transferred from Li [including the anion sites A_1 and A_2 in Fig. 2(b)] and Mg to H atoms. We further estimate the number of transferred electrons between the Li/Mg and H atoms by calculating the Bader charges [47] of Li_2MgH_{16}. Figure 3(d) shows the Bader basins of the constituent atoms, obtained from the gradient of the total charge density of Li_2MgH_{16} [47]. We find that the Bader charges inside Li, Mg, H_1, and H_2 basins are $-2.22e$, $-8.34e$, $-1.18e$, and $-1.28e$, respectively. Since this Bader charge of Li (Mg) includes $1s^2$ ($2s^22p^6$) core electrons, Li (Mg) atoms lose electrons of $0.78(1.66)e$ per atom, while H_1 (H_2) atoms gain electrons of $0.18(0.28)e$ per atom.

The charge transfer from Li dopants to H cages is expected to shift the Fermi level upward into the conduction band of the parent MgH_{16} system. To explore the rigid band shift due to such an electron doping, we compare the band structures of MgH_{16} and Li_2MgH_{16}, which are displayed in Figs. 4(a) and 4(b), respectively. The band dispersions of the two systems are generally similar to each other. As expected, we find that the empty conduction-band states of the MgH_{16} system are occupied by Li doping, thereby leading to a shift of E_F by ∼2.49 eV [see the arrow in Fig. 4(b)]. It is noteworthy that the Li-derived states show their highest local DOS (LDOS) peak at around 3.9 eV above E_F [see Fig. 4(b)], indicating that Li_2MgH_{16} is an electron-doped magnesium hydride via Li doping. Especially, the LDOS values of Li, Mg, H_1, and H_2 atoms at E_F are 0.8×10^{-3}, 1.2×10^{-3}, 2.5×10^{-3}, and 6.6×10^{-3} states/eV/Å^3, respectively [see Fig. 4(b)], indicating that the H-derived states are about 3−8 (2−5) times larger than Li (Mg)-derived states. Such large ratios of H-derived states in Li_2MgH_{16} are different from the cases of other high-T_c hydrides such as H_3S [11] and LaH_{10} [48] where the LDOS of H-derived states at E_F is nearly the same as those of S- and La-derived states, respectively. Such large H-derived electronic states near E_F should increase electron-phonon coupling [26], which leads to the highest T_c ever reported.

IV. CONCLUSION

Our first-principles DFT calculations have shown that the pyroclore-structured Li dopants exhibit an electride nature with anionic electrons ditributed in interstitial regions. Such loosely bound anionic electrons are easily captured to the H_{18} and H_{28} cages. We thus proposed that the electride nature of Li dopants importantly determines the charge transfer between Li dopants and H atoms. The present findings demonstrated that the anionic electrons created by Li dopants play important roles not only in stabilizing the clathrate H cages, but also in enhancing the H-derived DOS at E_F. It is noted that the presently proposed charge transfer mechanism can be applicable to compressed LaH_{10} [49] which was recently synthesized [20, 21] to exhibit the highest T_c so far among experimentally available superconducting materials. Here, the charge transfer from La to H atoms is driven by the electride property of the La framework at high pressure (see Fig. S6 in the Supplemental Material [39]). Therefore, the underlying mechanism of charge transfer in Li_2MgH_{16} would be more generic, and it will be useful for the discovery and design of new high-T_c hydrides in the future.

ACKNOWLEDGEMENTS

This work was supported by the National Research Foundation of Korea (NRF) grant funded by the Korean Government (Grants No. 2019R1A2C1002975, No. 2016K1A4A3914691, and No. 2015M3D1A1070609). The calculations were performed by the KISTI Supercomputing Center through the Strategic Support Program (Program No. KSC-2019-CRE-0183) for the supercomputing application research.

* Corresponding author: chojh@hanyang.ac.kr

[1] J. A. Flores-Livas, L. Boeri, A. Sanna, G. Profeta, R. Arita, and M. Eremets, Phys. Rep. **856**, 1 (2020), and references therein.
[2] N. W. Ashcroft, Phys. Rev. Lett. **21**, 1748 (1968).
[3] J. Bardeen, L. N. Cooper, and J. R. Schrieffer, Phys. Rev. **106**, 162 (1957).
[4] J. M. McMahon, M. A. Morales, C. Pierleoni, and D. M. Ceperley, Rev. Mod. Phys. **84**, 1607 (2012).
[5] J. McMinis, R. C. Clay, D. Lee, and M. A. Morales, Phys. Rev. Lett. **114**, 105305 (2015).
[6] R. P. Dias and I. F. Silvera, Science **355**, 715 (2017).
[7] P. Loubeyre1, F. Occelli1, and P.l Dumas, Nature **577**, 631 (2020).
[8] W. A. Bassett, High Press. Res. **29**, 163 (2009).
[9] H. K. Mao, X. J. Chen, Y. Ding, B. Li, and L. Wang, Rev. Mod. Phys. **90**, 015007 (2018).
[10] N. W. Ashcroft, Phys. Rev. Lett. **92**, 187002 (2004).
[11] D. Duan, Y. Liu, F. Tian, D. Li, X. Huang, Z. Zhao, H. Yu, B. Liu, W. Tian, and T. Cui, Sci. Rep. **4**, 6968 (2014).
[12] E. Zurek, R. Hoffmann, N. W. Ashcroft, A. R. Oganov, and A. O. Lyakhov, Proc. Natl. Acad. Sci. USA **106**, 42 (2009).
[13] Y. Xie, Q. Li, A. R. Oganov, and H. Wang, Acta Cryst. C**70** 104 (2014).
[14] J. Hooper and E. Zurek, J. Phys. Chem. C **116** 13322 (2012).
[15] H. Wang, J. S. Tse, K. Tanaka, T. Litaka, and Y. Ma, Proc. Natl. Acad. Sci. USA **109**, 6463 (2012).
[16] X. Feng, J. Zhang, G. Gao, H. Liu, and H. Wang, RSC Adv. **5**, 59292 (2015).
[17] F. Peng, Y. Sun, C. J. Pickard, R. J. Needs, Q. Wu, and Y. Ma, Phys. Rev. Lett. **119**, 107001 (2017).
[18] H. Liu, I. I. Naumov, R. Hoffmann, N. W. Ashcroft, and R. J. Hemley, Proc. Natl. Acad. Sci. USA **114**, 6990 (2017).
[19] A. P. Drozdov, M. I. Eremets, I. A. Troyan, V. Ksenofontov, and S. I. Shylin, Nature (London) **525**, 73 (2015).
[20] M. Somayazulu, M. Ahart, A. K. Mishra, Z. M. Geballe, M. Baldini, Y. Meng, V. V. Struzhkin, and R. J. Hemley, Phys. Rev. Lett. **122**, 027001 (2019).
[21] A. P. Drozdov, P. P. Kong, V. S. Minkov, S. P. Besedin, M. A. Kuzovnikov, S. Mozaffari, L. Balicas, F. F. Balakirev, D. E. Graf, V. B. Prakapenka, E. Greenberg, D. A. Knyazev, M. Tkacz, and M. I. Eremets, Nature (London) **569**, 528 (2019).
[22] C. M. Pépin, G. Geneste, A. Dewaele, M. Mezouar, and P. Loubeyre, Science **357**, 382 (2017).
[23] X. Li, X. Huang, D. Duan, C. J. Pickard, D. Zhou, H. Xie, Q. Zhuang, Y. Huang, Q. Zhou, B. Liu, and T. Cui, Nat. Commun. **10**, 3461 (2019).
[24] N. P. Salke, M. M. Davari Esfahani, Y. Zhang, I. A. Kruglov, J. Zhou, Y. Wang, E. Greenberg, V. B. Prakapenka, J. Liu, A. R. Oganov, and J.-F. Lin, Nat. Commun. **10**, 4453 (2019).
[25] E. Zurek and T. Bi, J. Chem. Phys. **150**, 050901 (2019).
[26] Y. Sun, J. Lv, Y. Xie, H. Liu, and Y. Ma, Phys. Rev. Lett. **123**, 097001 (2019).
[27] X. Liang, A. Bergara, L. Wang, B. Wen, Z. Zhao, X. F. Zhou, J. He, G. Gao, and Y. Tian, Phys. Rev. B **99**, 100505(R) (2019).
[28] Z. Shao, D. Duan, Y. Ma, H. Yu, H. Song, H. Xie, D. Li, F. Tian, B. Liu, and Tian Cui, Npj Comput. Mater. **5**, 104 (2019).
[29] M. Rahm, R. Cammi, N. W. Ashcroft, and R. Hoffmann, J. Am. Chem. Soc. **141**, 10253 (2019).
[30] M. Miao and R. Hoffman, J. Am. Chem. Soc. **137**, 3631 (2014).
[31] J. Wang, Q. Zhu, Z. Wang, and H. Hosono, Phys. Rev. B **99**, 064104 (2019) and referenes therein.
[32] Z. Zhao, S. Zhang, T. Yu, H. Xu, A. Bergara, and G. Yang, Phys. Rev. Lett. **122**, 097002 (2019).
[33] G. Kresse and J. Hafner, Phys. Rev. B **48**, 13115 (1993).
[34] G. Kresse and J. Furthmüller, Comput. Mater. Sci. **6**, 15 (1996).
[35] P. E. Blöchl, Phys. Rev. B **50**, 17953 (1994).
[36] J. P. Perdew, K. Burke, and M. Ernzerhof, Phys. Rev. Lett. **77**, 3865 (1996); **78**, 1396 (1997).
[37] P. Giannozzi, S. Baroni, N. Bonini, M. Calandra, R. Car, C. Cavazzoni, D. Ceresoli, G. L. Chiarotti, M. Cococcioni, I. Dabo *et al.*, J. Phys.: Condens. Matter **21**, 395502 (2009).
[38] M. Schlipf and F. Gygi, Comput. Phys. Commun. **196**, 36 (2015).
[39] See Supplemental Material at http://link.aps.org/supplemental/xxxxx for the H−H bond lengths of the H_{18} and H_{28} cages, the band structures of the parent MgH_{16} system and Li_2MgH_{16}, the electron localization function of the pyroclore-structured Li dopants, the valence charge densities of the isolated Li dopants with respect to pressure, the phonon spectra of MgH_{16} and Li_2MgH_{16}, and the anionic electrons in LaH_{10}.
[40] B. Silvi and A. Savin, Nature (London) **371**, 683 (1994).
[41] T. Tada, S. Takemoto, S. Matsuishi, and H. Hosono, Inorg. Chem. **53**, 10347 (2014).

[42] Y. Ysuji, P. L. V. K. Dasari, S. F. Elatresh, R. Hoffmann, and N. W. Ashcroft, J. Am. Chem. Soc. **138**, 14108 (2016).
[43] Y. Zhang, H. Wang, Y. Wang, L. Zhang, and Y. Ma, Phys. Rev. X **7**, 011017 (2017).
[44] Z. Lin, J. H. Choi, Q. Zhang, W. Qin, S. Yi, P. Wang, L. Li, Y. Wang, H. Zhang, Z. Sun, L. Wei, S. Zhang, T. Guo, Q. Lu, J.-H. Cho, C. Zeng, and Z. Zhang Phys. Rev. Lett. **121**, 096401 (2018).
[45] A. Mielke, J. Phys. A **24**, L73 (1991); *ibid*. **24**, 3311 (1991); *ibid*. **25**, 4335 (1992).
[46] E. Kaxiras, *Atomic and Electronic Structure of Solids.* Cambridge University Press, New York, pp 152 (2003).
[47] R. F. W. Bader, Acc. Chem. Res. **18**, 9 (1985).
[48] L. Liu, C. Wang, S. Yi, K. W. Kim, J. Kim, and J.-H. Cho, Phys. Rev. B **99**, 140501(R) (2019).
[49] S. Yi, C. Wang, H. Jeon, and J.-H. Cho, arXiv: 2007.01531.

Supplemental Material for Underlying mechanism of charge transfer in Li-doped MgH_{16} at high pressure

1. H-H bond lengths of the H_{18} and H_{28} cages

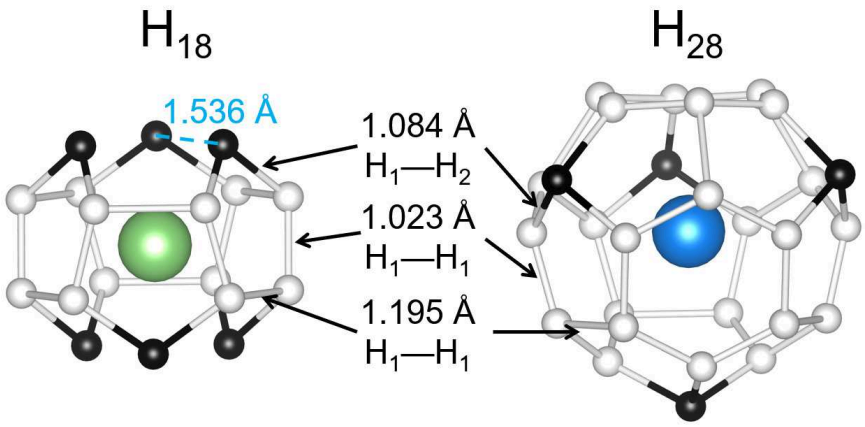

FIG. S1: Calculated H-H bond lengths of the H_{18} and H_{28} cages at 300 GPa. The H_{18} cage consisting of six pentagon rings is opened, but the H_{28} cage consisting of twelve pentagon and four hexagon rings has a closed shape.

2. Band structures of the pyroclore-structured Li dopants, MgH_{16}, and Li_2MgH_{16}

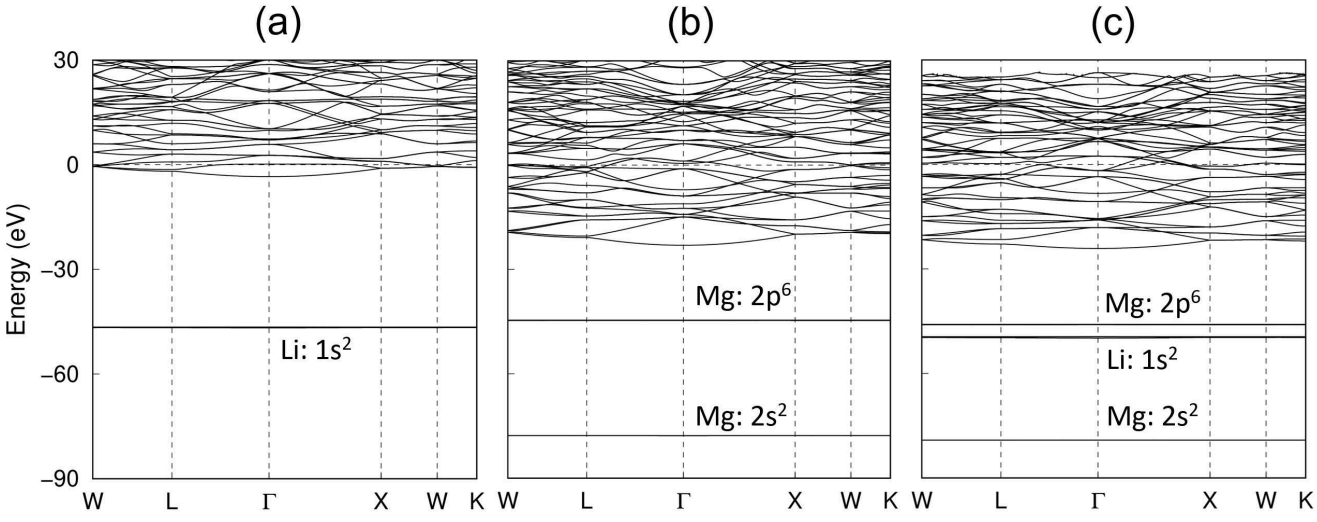

FIG. S2: Calculated band structures of (a) the pyroclore-structured Li dopants, (b) MgH_{16}, and (c) Li_2MgH_{16}. The electronic states of Li-$1s^2$ or/and Mg-$2s^2 2p^6$ are well separated from the valence states of each system.

3. Electron localization function of the pyroclore-structured Li dopants

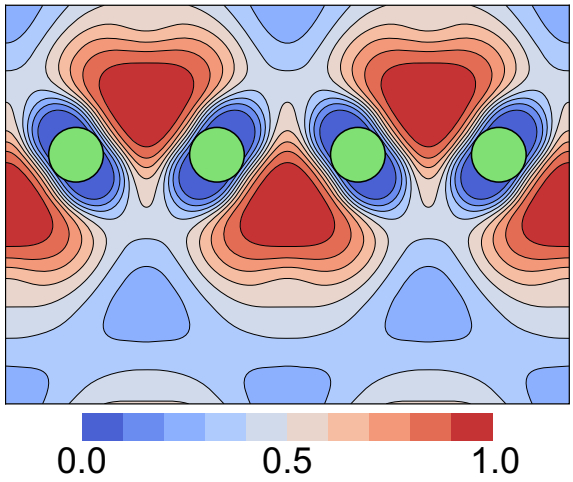

FIG. S3: Electron localization function of the pyroclore-structured Li dopants. This result indicates that some electrons are transferred from Li atoms to the interstitial regions around the A_1 and A_2 sites [see Fig. 2(b)].

4. Valence charge densities of the isolated Li dopants at 250, 300, and 350 GPa, respectively

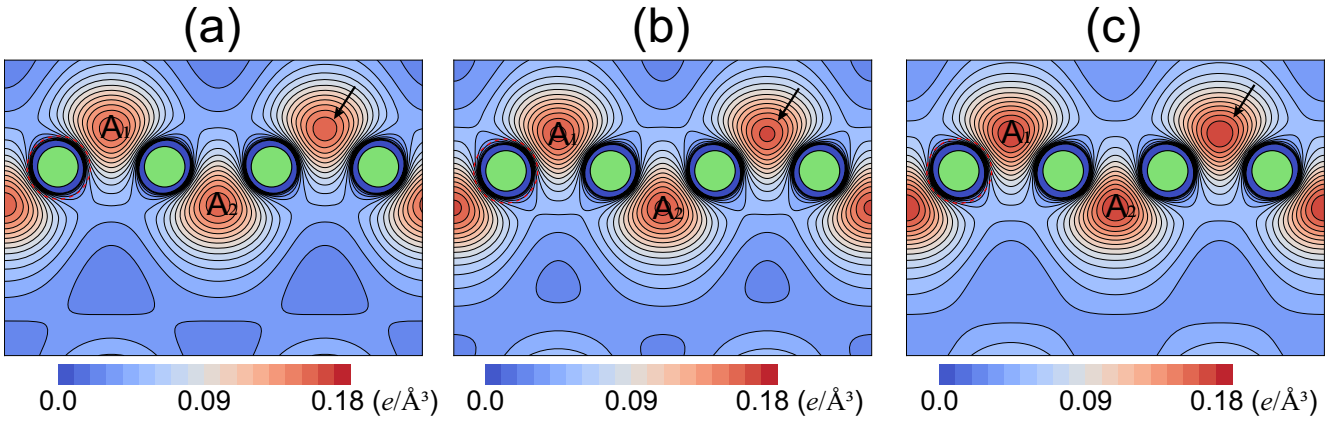

FIG. S4: Contour plots of valence charge density of the isolated Li dopants at (a) 250, (b) 300, and (c) 350 GPa. These plots are drawn on the (110) plane with a contour spacing of 0.01 e/Å^3. The black arrow indicates the charge density contour line of 0.15 e/Å^3.

5. Phonon spectra of MgH_{16} and Li_2MgH_{16}

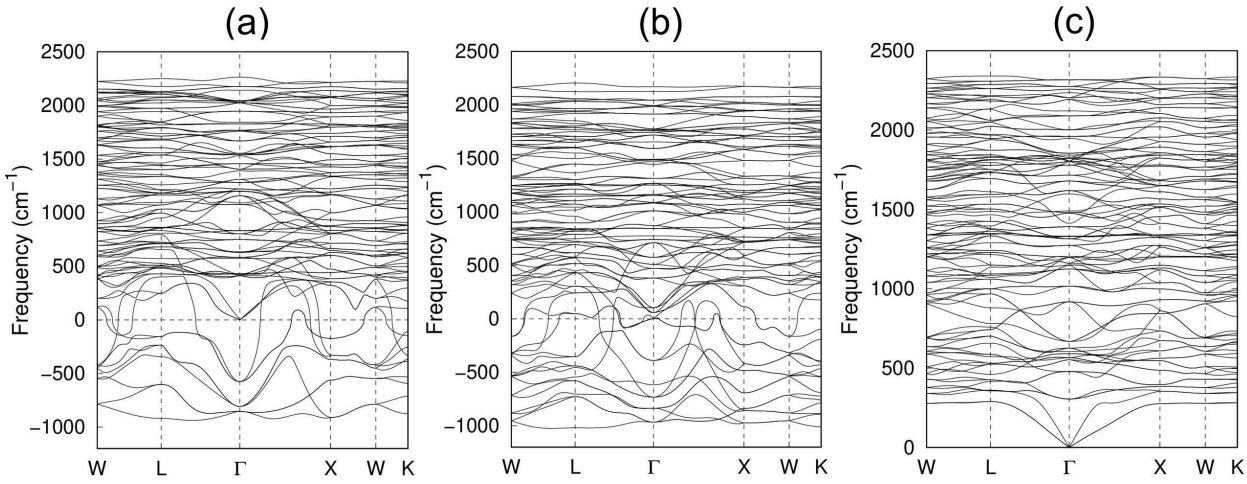

FIG. S5: Calculated phonon spectra of (a) MgH_{16}, (b) relaxed MgH_{16}, and (c) Li_2MgH_{16}. We find that MgH_{16} without Li atoms is dynamically unstable, while Li_2MgH_{16} is dynamically stable.

6. Structure of LaH_{10} and anionic electrons in the La lattice

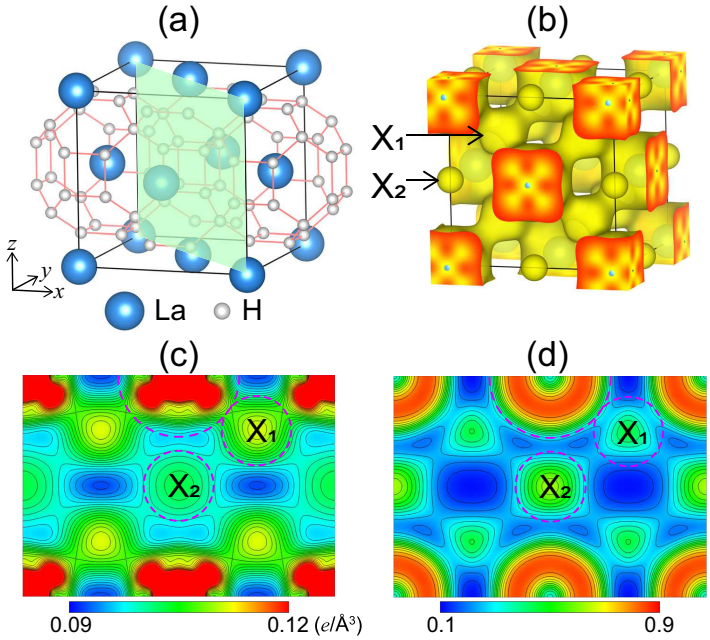

FIG. S6: Optimized structure of LaH_{10} at 300 GPa and (b) calculated charge density isosurface of valence electrons in the La lattice whose structure is taken from LaH_{10}. The charge density and electron localization function (ELF) of the La lattice are plotted on the (110) plane in (c) and (d), respectively. A (110) plane is drawn in (a). The isosurface in (b) is taken as 0.11 e/Å^3, and the contour spacings in (c) and (d) are 0.002 e/Å^3 and 0.05, respectively. In (b), X_1 and X_2 indicate the two anions in interstitial regions. The dashed circles in (c) represent the muffin-tin spheres around La, X_1 and X_2 with the radii of 1.31, 0.75 and 0.75 /Å, whithin which the electron numbers are 1.17e, 0.21e and 0.19e, respectively. Therefore, each La atom loses about 1.83 electrons, some of which are transferred to the interstitial regions around the X_1 and X_2 sites. The confinement of anionic electrons around the X_1 and X_2 sites is confirmed by the ELF [see T. Tada et al., Inorg. Chem. 53, 10347 (2014)]. It is thus likely that the charge transfer from La to H atoms in compressed LaH_{10} is driven by the electride property of the La lattice.